Flexural strike-slip basins

Derek Neuharth[1,2], Sascha Brune[1,2], Anne Glerum[1], Chris K. Morley[3], Xiaoping Yuan[4,1], Jean Braun[1,2]

[1]*GFZ German Research Centre for Geosciences, Telegrafenberg, 14473 Potsdam, Germany.*

[2]*Institute of Geosciences, University of Potsdam, Germany.*

[3]*PTTEP, Enco, Vibhavadi-Rangsit Road, Chatuchak, Bangkok, 10900, Thailand*

[4]*School of Earth Sciences, China University of Geosciences, Wuhan, China*

ABSTRACT

Strike-slip faults are classically associated with pull-apart basins where continental crust is thinned between two laterally offset fault segments. We propose a subsidence mechanism to explain the formation of a new type of basin where no substantial segment offset or syn-strike-slip thinning is observed. Such "flexural strike-slip basins" form due to a sediment load creating accommodation space by bending the lithosphere. We use a two-way coupling between the geodynamic code ASPECT and surface-processes code FastScape to show that flexural strike-slip basins emerge if sediment is deposited on thin lithosphere close to a strike-slip fault. These conditions were met at the Andaman Basin Central fault (Andaman Sea, Indian Ocean), where seismic reflection data provide evidence of a laterally extensive flexural basin with a depocenter located parallel to the strike-slip fault trace.

MOTIVATION

Near plate boundaries, accommodation space for sedimentary basins is created by (1) lithospheric stretching or cooling, which controls rift-basin formation at divergent boundaries, and (2) lithospheric flexure such as in foreland basins in convergent settings and cratonic sag basins in continental interiors (Allen and Allen, 2013). Pull-apart basins at transform plate boundaries are thought to be related to the first process.

Pull-apart basins form between laterally offset strike-slip fault segments (Mann et al., 1983; Gürbüz, 2010). During strike-slip motion, the area between the offset faults is extended and basement subsidence occurs in this area due to crustal thinning (van Wijk et al., 2017). Pull-apart basins lengthen over time and form as long thin basins with a depocenter that is bounded by the strike- or oblique-slip segments (Seeber et al., 2004). While there are many pull-apart basin examples (e.g., the Dead Sea Basin: Garfunkel and Ben-Avraham, 1996; Death Valley Basin: Serpa et al., 1988), there has not been much discussion on other types of strike-slip basins.

Flexural basins form when an overlying load deflects the lithosphere, e.g., during mountain building, where an orogenic load creates accommodation space for sediment infill. However, under conditions without an orogenic load, basement subsidence may be a consequence of lower-crustal flow triggered by enhanced sedimentation in deep basins (Morley and Westaway, 2006; Clift et al., 2015), e.g., the fans of the Red River (Clift and Sun, 2006) and Pearl River (Dong et al., 2020; both examples are located at the northern continental margin of the South China Sea).

We infer that the creation of sedimentation-induced accommodation space requires and is enhanced by (1) an easily deformable tectonic environment, and (2) focused sedimentation. Both can occur in regions of prior tectonic subsidence. Furthermore, because strike-slip faults may represent highly weakened plate boundaries (Zoback et al., 1987; Provost and Houston, 2003) and transform continental margins commonly follow a phase of thinning (Jourdon et al., 2021), we formulate the key hypothesis of this study: regions near strike-slip faults can represent a combination of factors whereby significant basement subsidence is driven by sedimentary loading. The positive feedback between focused sedimentation and flexural subsidence leads to the creation of a previously unrecognized type of basin that we term “flexural strike-slip basin”. We test our hypothesis by (1) numerical forward modeling of a strike-slip system subjected to asymmetric sedimentation, and (2) seismic reflection interpretation from the East Andaman Basin (EAB) in the Andaman Sea (Indian Ocean).

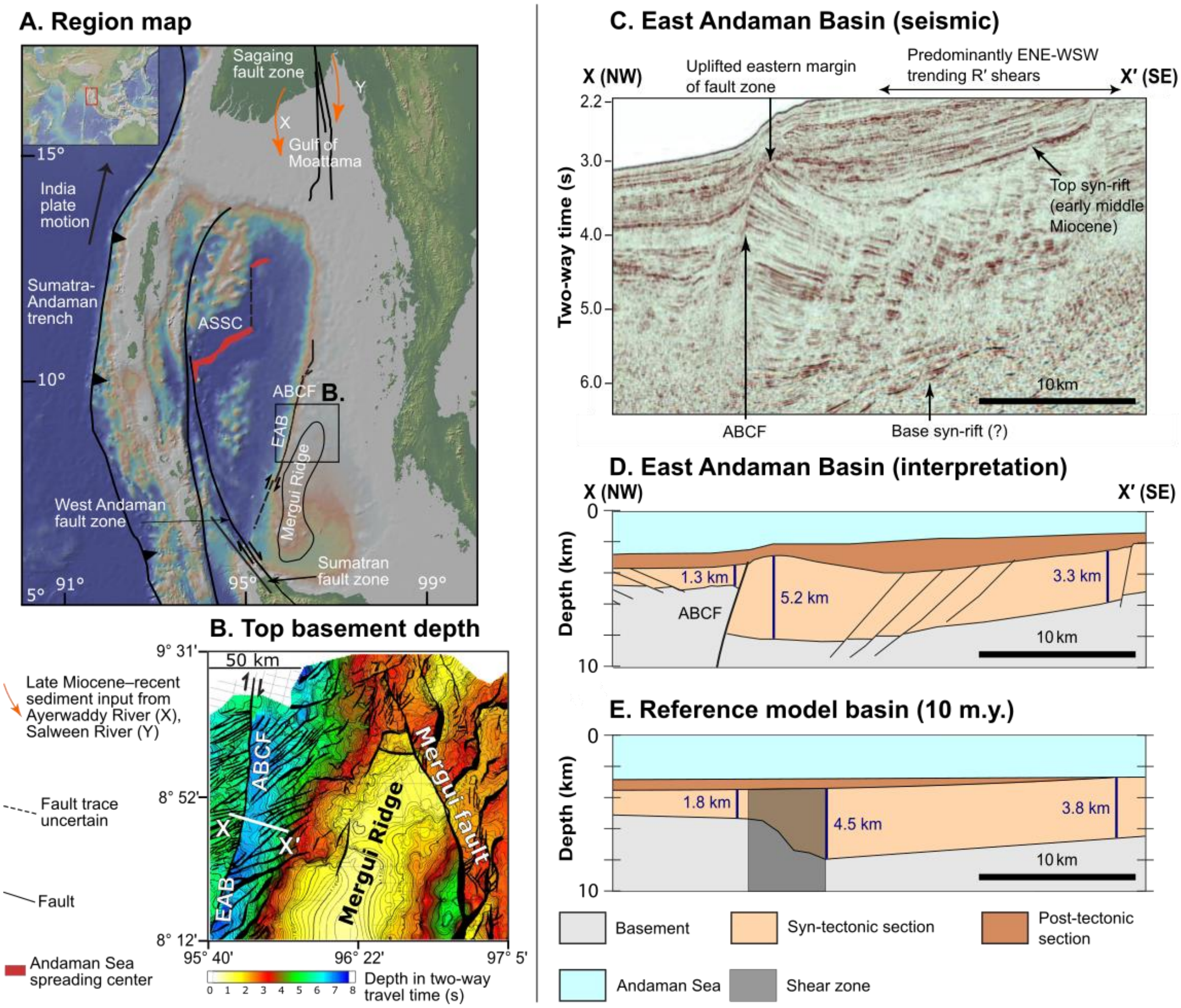

Figure 1. (A) Andaman Sea map. ASSC—Andaman Sea spreading center; ABCF—Andaman Basin Central fault; EAB—East Andaman Basin. (B) Depth to the top of the basement in two-way travel time. (C) Seismic data of the EAB. See B for profile location. (D) Depth interpretation of C. (E) Modeled basin. Post-tectonic sediment is computed by adding basement subsidence from 5 to 10 m.y. to the topography at 5 m.y.

GEOLOGICAL SETTING OF THE ANDAMAN SEA

During the Cenozoic, the Andaman Sea formed a transtensional backarc basin when India coupled with western Myanmar (Curray, 2005). Multiple strike-slip faults exist in the region, including the active, dextral, Sagaing fault (Fig. 1; 18 mm/yr: Vigny et al., 2003; Maurin et al., 2010) in the northeast of the Andaman Sea that connects southwestward to the Andaman spreading center (Curray, 2005). South of the Sagaing fault is the inactive Andaman Basin Central (strike-slip) fault (ABCF; Morley, 2016, 2017; Mahattanachai et al., 2021).

The Andaman Sea's transtensional motion led to subsidence and a submarine environment, causing the area to act as a sediment trap. Fault trends suggest the region near the ABCF experienced WNW-ESE extension in the Oligocene that shifted to NNW-SSE transtensional strike-slip motion during the early to mid-Miocene (lasting ~5 m.y.; Morley, 2017). The ABCF follows a previous necking zone of hyperextended continental crust (7–10 km thick; Morley, 2017; Mahattanachai et al., 2021). During strike-slip motion, the easterly Mergui Ridge was partially subaerial and, along with peninsular Thailand, acted as an asymmetric clastic sediment source for the EAB located along the ABCF (Mahattanachai et al., 2021).

The geometry of the EAB in relation to the ABCF is described in detail by Mahattanachai et al. (2021), who concluded that the long (>200 km), deep (>4 km), westward-thickening basin on the east side of the sub-vertical fault did not fit classic extensional or pull-apart basin characteristics.

MODEL SETUP AND EVOLUTION

We reproduce the key aspects of the ABCF region, namely that of a submarine environment, thin lithosphere, and asymmetric sedimentation, using a viscoplastic 100 × 8 × 120 km (*X*, *Y*, *Z*) three-dimensional box model via a two-way coupling of the tectonic code ASPECT (https://aspect.geodynamics.org, version 2.3.0-pre, commit 886749d) (Figs. 2B and 2C; Kronbichler et al., 2012; Heister et al., 2017; Glerum et al., 2018; Bangerth et al., 2019; Text S1 in the Supplemental Material) and the surface-processes code FastScape (https://fastscape.org) (Braun and Willett, 2013; Yuan et al., 2019b, 2019a; Text S2). We assume that a previous extensional event left the region submarine with thinned, 40-km-thick lithosphere. The model is initialized with 4 km of upper crust, 4 km of lower crust, 32 km of mantle lithosphere, and 80 km of asthenosphere (Fig. 2B; Fig. S1 in the Supplemental Material). The eastern boundary (right edge in Fig. 2B) has no slip in any direction, the western boundary (left edge in Fig. 2B) has no slip in the *Z* direction, 20 mm/yr in the *Y* direction to induce strike-slip motion, and is given a small (0.2 mm/yr) extensional component in the *X* direction that helps avoid bending-induced compression but does not affect the presented results (Fig. S2). To simulate an infinitely long strike-slip fault with minimal along-strike variation, the northern and southern boundaries are periodic, in that any material advected out of the northern boundary will flow into the model from the southern boundary, or vice-versa.

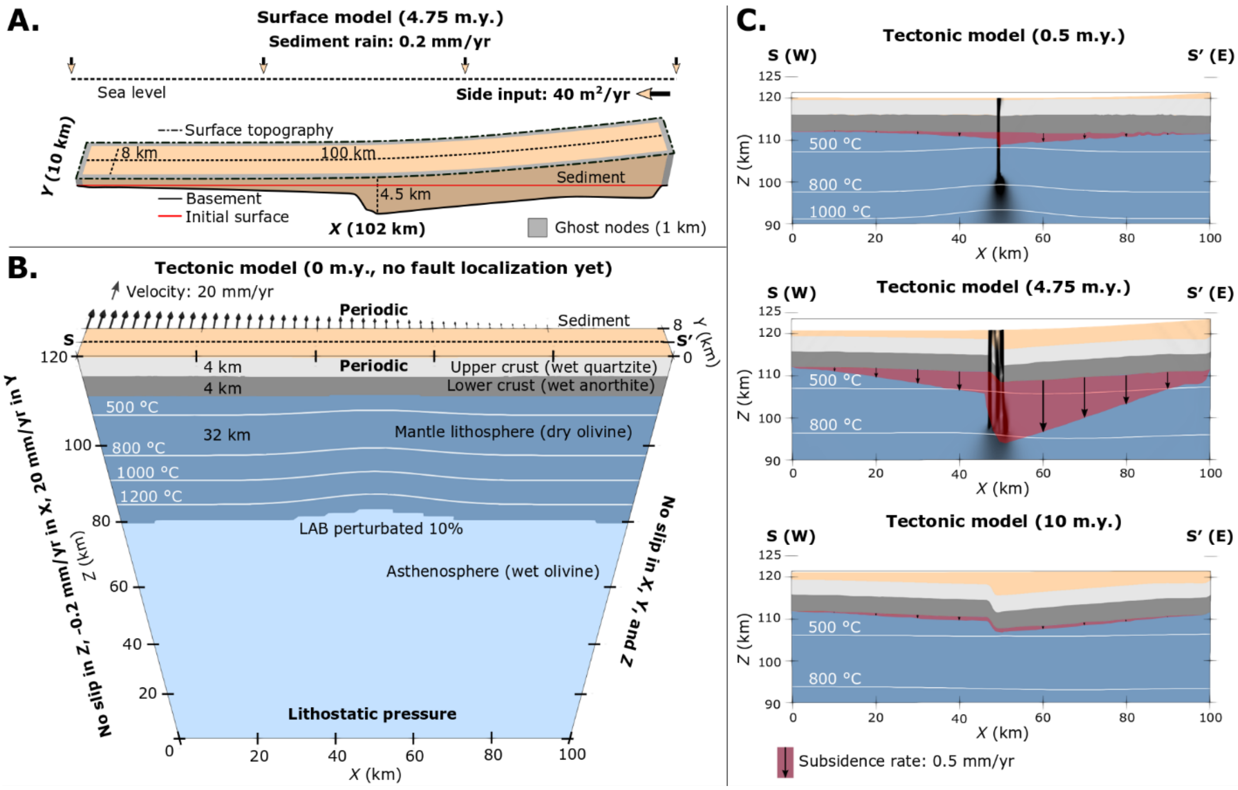

Figure 2. (A) Surface-processes model at 4.75 m.y. and 2× vertical exaggeration. Sediment (beige) is the area between topography (dash-dot line) and basement (solid black line). Ghost nodes (gray) are a single cell-size (1 km in *X* and *Y*) layer surrounding the surface processes model implemented for periodic advection along the *Y* direction and to control sedimentary side input, surround the surface model and do not interact with the tectonic model. (B) Initial tectonic setup. Colors represent composition; white isotherms represent temperature distribution. Arrows indicate total velocity magnitude. The northern and southern boundaries are periodic, indicating that material flow out one boundary will become inflow on the opposing boundary. LAB—lithosphere-asthenosphere boundary. (C) Cross sections of the top 30 km of the tectonic model along S-S′ in B showcase the formation of a flexural strike-slip basin in response to sedimentation. Subsidence rate at the Moho is indicated in red. See Movies S1 and S2 in the Supplemental Material.

The initial lithostatic pressure at a reference location is prescribed on the bottom boundary to allow for outflow in response to sedimentation. The strike-slip fault forms self-consistently above an initial perturbation of the lithosphere-asthenosphere boundary (10% reduction of lithosphere thickness) in the center of the model that acts as a weak zone for deformation to localize. Accumulated plastic strain over an interval of 0–1 weakens the angle of friction from an initial value of 30° to a final value of 7.5°, promoting brittle localization.

The surface-processes code FastScape is coupled to the top of the tectonic model (Text S3). The model is submarine and sediment is transported via diffusion with a coefficient of 500 m^2/yr, consistent with open-marine environments in previous modeling studies (Rouby et al., 2013). Sediment is supplied to the domain in two ways: (1) the entire surface experiences 0.2 mm/yr of pelagic and/or hemipelagic "sediment rain" sedimentation; and (2) ghost nodes (Fig. 2A) at the eastern boundary are uplifted each time step to prescribe a constant sediment flux of 40 m^2/yr, mimicking an off-model sediment source similar to the Mergui Ridge for the EAB.

The models are run for 10 m.y., where the first 5 m.y. represent the syn-tectonic stage with strike-slip motion and sedimentation to mimic the ~5 m.y. during which the ABCF was active. The final 5 m.y. constitute the post-tectonic stage with no prescribed motion or sediment supply, although sediment transport continues (for setup details, see Text S4).

REFERENCE MODEL RESULTS

In the reference model, strain localizes on a vertical fault near the model center (at ~0.5 m.y.; Fig. 2C). Both sides of the fault subside due to the influx of sediment, with the eastern side sinking faster (1.0 versus 0.4 mm/yr at 4.75 m.y.). By 5 m.y., the eastern side has subsided more than the western side (3.6 versus 1.0 km), rotating the strike-slip fault to subvertical. After strike-slip motion and sedimentation have ceased, the subsidence rate declines to 0.08 mm/yr as the sediment hill at the eastern boundary is distributed across the surface. By 10 m.y., both sides have subsided another 0.4 km, showing a synformal thickening geometry along the fault.

The model indicates that a flexural strike-slip basin emerges due to sedimentation above thin lithosphere close to a strike-slip fault, wherein the fault acts as a weak zone where subsidence focuses. In contrast to classical half-graben or pull-apart geometries, these basins form without a significant extensional component (i.e., without crustal thinning as seen in pull-apart basins).

CONTROLS ON FLEXURAL STRIKE-SLIP BASIN FORMATION

To test controls on flexural strike-slip basin formation, we ran a series of models varying in sedimentation rate, lithospheric thickness, and fault strength. Sedimentation rate was changed by altering the eastern-side influx from 0 (i.e., only sediment rain) to 60 m^2/yr (Figs. 3A–3D). With no lateral input, both sides subsided evenly, forming a synformal basin that is thickest at the fault (Fig. 3A). This suggests that reference-model basin asymmetry is affected primarily by sedimentation and not by the initial perturbation. At higher lateral input, the eastern side subsided more, from a maximum basement deflection of 0.9 km with no input to 5.7 km for 60 m^2/yr of input (Fig. 3D). The western side shows a less-pronounced deflection with higher sediment input (0.8–1.6 km), suggesting either that the sides are not fully decoupled or that more sediment reached the western side.

The effects of varying the lithospheric thickness from 60 to 30 km (Figs. 3E–3H) reduce the basement flexural deflection on the eastern side of the fault from 4.6 km at 30 km to 1.4 km at 60 km, suggesting that deep flexural basins are unlikely to form in regions with thick lithosphere.

The final key variable is friction-angle weakening (Figs. 3I–3L). This shows that fault strength affects flexural subsidence (4.2 versus 3.3 km deflection at 99% and 25% weakening, respectively), suggesting that regions with no weakening or without strike-slip motion (Fig. S3) would experience much less subsidence. Further, weak faults promote lithospheric decoupling and basin asymmetry related to asymmetric sedimentation.

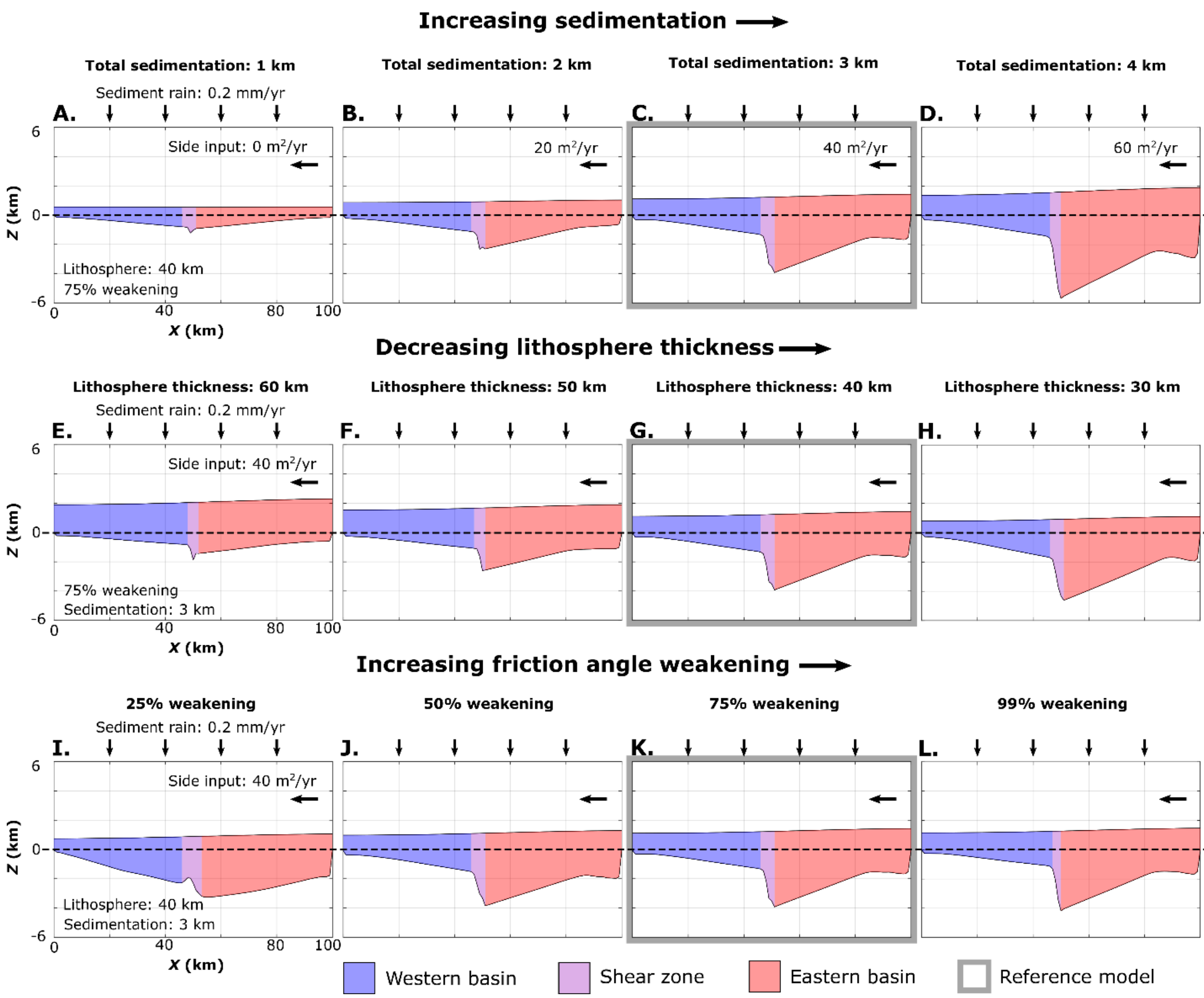

Figure 3. Modeled basin formation when subject to variable sediment input (A–D), lithosphere thickness (E–H), and fault weakening (I–L). Dashed lines along *Z* = 0 show initial model elevation. Total sedimentation is sediment thickness assuming an even distribution across the model.

FLEXURAL STRIKE-SLIP BASINS IN THE ANDAMAN SEA

Seismic data suggest that the EAB is an asymmetric basin that spans both sides of the ABCF (Mahattanachai et al., 2021). On the western side, basin thickness is fairly uniform (1–2 km; Fig. 1D). Along the fault on the eastern side, the basin is substantially thicker (∼5 km) and thins eastward toward the sediment source areas of the Mergui Ridge and peninsular Thailand.

The Gulf of Moattama Basin formed along the active Sagaing fault and is a more ambiguous example where a deep (>10 km) depocenter formed in the past ∼6 m.y., although strike-slip fault activity in the area probably dates to the Oligocene (Morley and Arboit, 2019). Although a gentle releasing-bend geometry is present in the offshore fault trace, the basin did not undergo dramatic subsidence until the latest Miocene–Pliocene, when a major transgression followed structural uplift and inversion of basins onshore (e.g., Morley and Alvey, 2015). We suggest the axial sediment influx along the Gulf of Moattama Basin resulted in the flexural strike-slip mechanism enhancing the effects of the fault geometry.

The primary requirement for flexural strike-slip basin formation is weak or thin lithosphere and high sedimentation rates. There are two basin types, controlled by the sedimentation pattern: (1) symmetric, where both sides receive a similar sediment load (Fig. 3A); and (2) asymmetric, where the two distinct basin sides subside at different rates dependent on the sediment load they receive (Fig. 3C). In both types, the maximum flexure and basin depocenter occur along the fault trace and the basin thins strike-perpendicularly.

The Andaman Sea provides likely examples for each flexural strike-slip basin type:

(1) The Gulf of Moattama Basin, where northern axial sedimentation provided even sedimentation to each side of the fault and formed a *symmetric flexural basin*. While sedimentation was not purely uniform, a synformal geometry developed centered along the fault zone, as in Figure 3A.

(2) The EAB (Fig. 1D), where perpendicular sedimentation from the east forced greater flexure on the eastern side of the fault, forming an *asymmetric flexural basin*. The EAB and reference model basin both have a change in sediment thickness across the fault and basin thinning toward the sediment source. Furthermore, basin thicknesses (excluding post-tectonic sediment) along the

fault’s eastern side (4.5 versus 5.2 km in the model and EAB, respectively) and western side (1.8 versus 1.3 km) are comparable between the model and the basin.

Despite the similarities, there are discrepancies between the modeled basin and the EAB. Eastward thinning of the sediment layer is less pronounced in the model. Given that the basement slope is affected by the lithosphere thickness and sediment load, three possible explanations are:

(1) The ABCF is capped by a regional unconformity with the post-tectonic sediments (Srisuriyon and Morley, 2014; Morley, 2017), and the fault may have received more sediment while active than expected from the seismic data.

(2) Given that the fault formed within a necking zone and the lithosphere thickness is not well constrained, the lithosphere may have varied spatially (rheologically or in thickness) and been thinner than the 40 km value used here.

(3) A more significant syn-strike-slip extensional component would have further deepened the basin along the fault (Sobolev et al., 2005).

Also, our models do not consider basin translation with strike-slip motion. This is justified by comparison with the EAB, where the thicker eastern basin is located on the same side as the Mergui Ridge and is not affected by the translation. For the western basin, the ∼350-km-long Mergui Ridge is longer than the total dextral strike-slip translation of ∼90 km from the early to mid-Miocene.

We focused on the Andaman Sea, but the key requirements for flexural strike-slip basins—thin lithosphere, focused sedimentation, and a weak fault—are possibly also met in the New Guinea Basin in the Bismarck Sea (southwestern Pacific Ocean; Fig. S4; Martinez and Taylor, 1996) and the Yinggehai Basin in the South China Sea (Fig. S5; Clift and Sun, 2006), although new seismic data are needed to test this. Another candidate is the Navassa Basin in the Jamaica Passage (Caribbean Sea; Fig. S6; Corbeau et al., 2016), an asymmetric strike-slip basin that is not located between offset segments. The basin likely formed during strike-slip motion and does not contain older sedimentary units found in nearby basins along the fault.

CONCLUSION

Our study suggests a new class of flexural basins that form along strike-slip faults. These basins are characterized by a fault-parallel depocenter and sediment that thins strike-perpendicularly. The basins can be classified in two types, which are both represented in the Andaman Sea: (1) *symmetric flexural basins*, where axial sedimentation causes a synformal shape, as seen in the Gulf of Moattama Basin; and (2) *asymmetric flexural basins*, where asymmetric sedimentation forces one basin side to subside more than the other, as seen in the EAB.

Flexural strike-slip basins form due to a strike-slip fault that acts as a weak zone facilitating differential subsidence due to sediment loading. The fault decouples the lithosphere sides, allowing them to respond independently to the sediment load they receive, determining basin symmetry. For a flexural strike-slip basin to form, two criteria must be met: the strike-slip fault must (1) cut through thin lithosphere, and (2) be subjected to a sufficient tectonic load.

ACKNOWLEDGMENTS

This study was conducted within the Helmholtz Young Investigators Group CRYSTALS (grant VH-NG-1132). We thank the Computational Infrastructure for Geodynamics (https://geodynamics.org/), which is funded by the U.S. National Science Foundation under awards EAR-0949446 and EAR-1550901, for supporting the development of ASPECT code. The work was supported by the North-German Supercomputing Alliance (HLRN, https://www.hlrn.de/). Software and input files are found at http://doi.org/10.5281/zenodo.4893421. Figures were made using ParaView, InkScape, and GeoMapApp. We also thank Anthony Jourdon, Zhen Sun, and an anonymous reviewer for their helpful reviews.

REFERENCES

Allen, P.A., and Allen, J.R., 2013, Basin Analysis 3rd edition:, doi:10.1017/CBO9781107415324.004.

Bangerth, W., Dannberg, J., Gassmoeller, R., and Heister, T., 2019, ASPECT v2.1.0: Zenodo, https://doi.org/10.5281/zenodo.2653531.

Braun, J., and Willett, S.D., 2013, A very efficient O(n), implicit and parallel method to solve the stream power equation governing fluvial incision and landscape evolution: Geomorphology, v. 180–181, p. 170–179, doi:10.1016/J.GEOMORPH.2012.10.008.

Clift, P.D., Brune, S., and Quinteros, J., 2015, Climate changes control offshore crustal structure at South China Sea continental margin: Earth and Planetary Science Letters, v. 420, p. 66–

72, doi:10.1016/j.epsl.2015.03.032.

Clift, P.D., and Sun, Z., 2006, The sedimentary and tectonic evolution of the Yinggehai-Song Hong basin and the southern Hainan margin, South China Sea: Implications for Tibetan uplift and monsoon intensification: Journal of Geophysical Research: Solid Earth, v. 111, p. 1–28, doi:10.1029/2005JB004048.

Corbeau, J., Rolandone, F., Leroy, S., Mercier de Lépinay, B., Meyer, B., Ellouz-Zimmermann, N., and Momplaisir, R., 2016, The northern Caribbean plate boundary in the Jamaica Passage: Structure and seismic stratigraphy: Tectonophysics, v. 675, p. 209–226, doi:10.1016/j.tecto.2016.03.022.

Curray, J.R., 2005, Tectonics and history of the Andaman Sea region: Journal of Asian Earth Sciences, v. 25, p. 187–232, doi:10.1016/j.jseaes.2004.09.001.

Dong, M., Zhang, J., Brune, S., Wu, S., Fang, G., and Yu, L., 2020, Quantifying Postrift Lower Crustal Flow in the Northern Margin of the South China Sea: Journal of Geophysical Research: Solid Earth, v. 125, doi:10.1029/2019JB018910.

Garfunkel, Z., and Ben-Avraham, Z., 1996, The structure of the Dead Sea basin: Tectonophysics, v. 266, p. 155–176, doi:10.1016/S0040-1951(96)00188-6.

Glerum, A., Thieulot, C., Fraters, M., Blom, C., and Spakman, W., 2018, Nonlinear viscoplasticity in ASPECT: Benchmarking and applications to subduction: Solid Earth, v. 9, p. 267–294, doi:10.5194/se-9-267-2018.

Gurbuz, A., 2010, Geometric characteristics of pull-apart basins: Lithosphere, v. 2, p. 199–206, doi:10.1130/L36.1.

Heister, T., Dannberg, J., Gassmöller, R., and Bangerth, W., 2017, High Accuracy Mantle Convection Simulation through Modern Numerical Methods – II: Realistic Models and Problems.: Geophysical Journal International, v. 210, p. 833–851, doi:doi:10.1093/gji/ggx195.

Jourdon, A., Kergaravat, C., Duclaux, G., and Huguen, C., 2021, Looking beyond kinematics: 3D thermo-mechanical modelling reveals the dynamics of transform margins: Solid Earth, v. 12, p. 1211–1232, doi:10.5194/se-12-1211-2021.

Kronbichler, M., Heister, T., and Bangerth, W., 2012, High Accuracy Mantle Convection Simulation through Modern Numerical Methods.: Geophysical Journal International, v. 191, doi:doi:10.1111/j.1365-246x.2012.05609.x.

Mahattanachai, T., Morley, C.K., Charusiri, P., and Kanjanapayont, P., 2021, The Andaman Basin Central Fault Zone, Andaman Sea: Characteristics of a major deepwater strike-slip fault system in a polyphase rift: Marine and Petroleum Geology, p. 104997, doi:10.1016/j.marpetgeo.2021.104997.

Mann, P., Hempton, M.R., Dwight, C.B., and Burke, K., 1983, Development of Pull-Apart Basins Authors: Paul Mann , Mark R . Hempton , Dwight C . Bradley and Kevin Burke Published by : The University of Chicago Press Stable URL : http://www.jstor.org/stable/30064017 . All use subject to JSTOR Terms and Conditio: The Journal of Geology, v. 91, p. 529–554.

Martinez, F., and Taylor, B., 1996, Backarc spreading, rifting, and microplate rotation, between transform faults in the Manus Basin: Marine Geophysical Researches, v. 18, p. 203–224, doi:10.1007/BF00286078.

Maurin, T., Masson, F., Rangin, C., Min, U.T., and Collard, P., 2010, First global positioning system results in northern Myanmar: Constant and localized slip rate along the Sagaing fault: Geology, v. 38, p. 591–594, doi:10.1130/G30872.1.

Morley, C.K., 2017, Cenozoic rifting, passive margin development and strike-slip faulting in the Andaman Sea: A discussion of established v. New tectonic models: Geological Society Memoir, v. 47, p. 27–50, doi:10.1144/M47.4.

Morley, C.K., 2016, The impact of multiple extension events, stress rotation and inherited fabrics on normal fault geometries and evolution in the Cenozoic rift basins of Thailand: Geological Society, London, Special Publications, v. 439, p. 413–445, doi:https://doi.org/10.1144/SP439.3.

Morley, C.K., and Alvey, A., 2015, Is spreading prolonged, episodic or incipient in the Andaman Sea? Evidence from deepwater sedimentation: Journal of Asian Earth Sciences, v. 98, p. 446–456, doi:10.1016/j.jseaes.2014.11.033.

Morley, C.K., and Arboit, F., 2019, Dating the onset of motion on the Sagaing fault: Evidence from detrital zircon and titanite U-Pb geochronology from the North Minwun Basin, Myanmar: Geology, v. 47, p. 581–585, doi:10.1130/G46321.1.

Morley, C.K., and Westaway, R., 2006, Subsidence in the super-deep Pattani and Malay basins of Southeast Asia: A coupled model incorporating lower-crustal flow in response to post-rift sediment loading: Basin Research, v. 18, p. 51–84, doi:10.1111/j.1365-2117.2006.00285.x.

Provost, A.-S., and Houston, H., 2003, Stress orientations in northern and central California: Evidence for the evolution of frictional strength along the San Andreas plate boundary system: Journal of Geophysical Research: Solid Earth, v. 108, p. 1–18, doi:10.1029/2001jb001123.

Rouby, D., Braun, J., Robin, C., Dauteuil, O., and Deschamps, F., 2013, Long-term stratigraphic evolution of Atlantic-type passive margins: A numerical approach of interactions between surface processes, flexural isostasy and 3D thermal subsidence: Tectonophysics, v. 604, p. 83–103, doi:10.1016/j.tecto.2013.02.003.

Seeber, L., Emre, O., Cormier, M.H., Sorlien, C.C., McHugh, C.M.G., Polonia, A., Ozer, N., and Cagatay, N., 2004, Uplift and subsidence from oblique slip: The Ganos-Marmara bend of the North Anatolian Transform, Western Turkey: Tectonophysics, v. 391, p. 239–258, doi:10.1016/j.tecto.2004.07.015.

SERPA, L., DE VOOGD, B., WRIGHT, L., WILLEMIN, J., OLIVER, J., HAUSER, E., and TROXEL, B., 1988, Structure of the central Death Valley pull-apart basin and vicinity from COCORP profiles in the southern Great Basin: GSA Bulletin, v. 100, p. 1437–1450, doi:10.1130/0016-7606(1988)100<1437:SOTCDV>2.3.CO;2.

Sobolev, S. V., Petrunin, A., Garfunkel, Z., and Babeyko, A.Y., 2005, Thermo-mechanical model of the Dead Sea Transform: Earth and Planetary Science Letters, v. 238, p. 78–95, doi:10.1016/j.epsl.2005.06.058.

Srisuriyon, K., and Morley, C.K., 2014, Pull-apart development at overlapping fault tips: Oblique rifting of a Cenozoic continental margin, northern Mergui Basin, Andaman Sea: Geosphere, v. 10, p. 80–106, doi:10.1130/GES00926.1.

Vigny, C., Socquet, A., Rangin, C., Chamot-Rooke, N., Pubellier, M., Bouin, M.-N., Bertrand, G., and Becker, M., 2003, Present-day crustal deformation around Sagaing fault, Myanmar: Journal of Geophysical Research: Solid Earth, v. 108, doi:https://doi.org/10.1029/2002JB001999.

van Wijk, J., Axen, G., and Abera, R., 2017, Initiation, evolution and extinction of pull-apart basins: Implications for opening of the Gulf of California: Tectonophysics, v. 719–720, p. 37–50, doi:10.1016/j.tecto.2017.04.019.

Yuan, X.P., Braun, J., Guerit, L., Rouby, D., and Cordonnier, G., 2019a, A New Efficient Method to Solve the Stream Power Law Model Taking Into Account Sediment Deposition: Journal of Geophysical Research: Earth Surface, v. 124, p. 1346–1365, doi:10.1029/2018JF004867.

Yuan, X.P., Braun, J., Guerit, L., Simon, B., Bovy, B., Rouby, D., Robin, C., and Jiao, R., 2019b, Linking continental erosion to marine sediment transport and deposition: A new implicit and O(N) method for inverse analysis: Earth and Planetary Science Letters, v. 524, p. 115728, doi:10.1016/j.epsl.2019.115728.

Zoback, M.D. et al., 1987, New evidence on the state of stress of the san andreas fault system: Science, v. 238, p. 1105–1111, doi:10.1126/science.238.4830.1105.

Supplementary Information

Flexural strike-slip basins

Derek Neuharth[1,2], Sascha Brune[1,2], Anne Glerum[1], Chris K. Morley[3], Xiaoping Yuan[4,1], Jean Braun[1,2]

[1]GFZ German Research Centre for Geosciences, Telegrafenberg, 14473 Potsdam, Germany.

[2]Institute of Geosciences, University of Potsdam, Germany.

[3]PTTEP, Enco, Vibhavadi-Rangsit Road, Chatuchak, Bangkok, 10900, Thailand

[4]School of Earth Sciences, China University of Geosciences, Wuhan, China

Contents of this file

Additional supporting information (uploaded separately)

Text S1: ASPECT Methods

1.1 Governing equations

We perform numerical simulations of a 3D strike-slip system using the open source finite-element code ASPECT (Advanced Solver for Problems in Earth's ConvecTion, version 2.3.0-pre, commit 886749d; Heister et al., 2017; Kronbichler et al., 2012; Rose et al., 2017; Bangerth et al., 2019). ASPECT solves the following incompressible conservation equations assuming an infinite Prandtl number (i.e., without the inertial term),

$$-\nabla \cdot (2\eta\dot{\varepsilon}) + \nabla P = \rho\mathbf{g}\,, \tag{1}$$

$$\nabla \cdot (\mathbf{u}) = 0\,, \tag{2}$$

$$\bar{\rho}C_p\left(\frac{\partial T}{\partial t} + \mathbf{u} \cdot \nabla T\right) - \nabla \cdot k\nabla T = \bar{\rho}H + \alpha T\,(\mathbf{u} \cdot \nabla P)\,, \tag{3}$$

$$\frac{\partial c_i}{\partial t} + \mathbf{u} \cdot \nabla c_i = q_i\,, \tag{4}$$

where equation (1) represents the conservation of momentum, with η the effective viscosity, $\dot{\varepsilon}$ the deviator of the strain rate tensor (defined as $\frac{1}{2}(\nabla\mathbf{u} + (\nabla\mathbf{u})^T)$), $\mathbf{u}$ the velocity, P the pressure, ρ the density, and $\mathbf{g}$ gravity. Equation (2) describes the conservation of volume. Equation (3) represents the conservation of energy where $\bar{\rho}$ is the reference adiabatic density, C_p the specific heat capacity, T the temperature, k the thermal conductivity, H the radiogenic heating, and α the thermal expansivity. As right-hand-side heating terms, we include radioactive heating and adiabatic heating, in that order. Finally, we solve the advection equation (4) for each compositional field c_i (e.g., upper crust, lower crust, and accumulated plastic strain) with reaction rate q_i nonzero only for the plastic strain field.

1.2 Rheology

We use a visco-plastic rheology (Glerum et al., 2018), which additionally includes plastic weakening based on accumulated plastic strain. In the viscous regime, we use a composite of diffusion and dislocation creep (Karato and Wu, 1993), formulated as:

$$\eta_{\mathrm{eff}}^{\mathrm{diff|dis}} = \frac{1}{2} A_{\mathrm{diff|dis}}^{\frac{-1}{n}} d^{m} \dot{\varepsilon}_{e}^{\frac{1-n}{n}} \exp\left(\frac{(E_{\mathrm{diff|dis}} + PV_{\mathrm{diff|dis}})}{nRT}\right), \quad (5)$$

where A is a scalar prefactor, d the grain size, $\dot{\varepsilon}_e$ the square root of second invariant of the deviatoric strain rate, E the activation energy, P the pressure, V the activation volume, R the gas constant, T the temperature, and n the stress exponent. For diffusion, n = 1 and the equation becomes independent of strain rate. For dislocation creep, the grain size exponent m vanishes, rendering dislocation creep independent of grain size. Values for A, E, V, and n used in our models are composition-dependent and can be found in supplementary Table S1.

In the plastic regime, when viscous stresses exceed the yield stress, we use the Drucker-Prager yield criterion (Davis and Selvadurai, 2002). The effective plastic viscosity is given by

$$\eta_{\mathrm{eff}}^{\mathrm{pl}} = \frac{\frac{6C\cos\phi}{\sqrt{3}(3-\sin\phi)} + \frac{6P\sin\phi}{\sqrt{3}(3-\sin\phi)}}{2\dot{\varepsilon}_e}, \quad (6)$$

where C is the cohesion and ϕ the internal angle of friction. The accumulation of plastic strain is tracked as a compositional field. This field is used to linearly weaken ϕ from an initial value of 30° to a final value of 7.5° over the accumulated plastic strain interval of 0 to 1. The time-integrated value of the strain reaction rate q_i is approximated as $\dot{\varepsilon}_e \cdot dt$ when plastic yielding occurs (with dt the current timestep size).

Text S2: FastScape Methods

FastScape is a landscape evolution code that changes the topographic surface through uplift, advection, the stream-power law, and hillslope diffusion (Braun and Willett, 2013). It can additionally deposit fluvial sediment (Yuan et al., 2019a) and include a marine component, which handles marine sediment (sand/silt) transport and deposition, and layer compaction based on sand/silt porosity (Yuan et al., 2019b). It uses a 2D horizontal mesh with a uniform resolution. For simplicity, we here assume that the entire model surface is submarine, with uniform properties (i.e., sand and silt transport coefficients are the same), and that there is no compaction (porosity is zero). Hence, FastScape deforms the surface through the uplift rate and marine diffusion equation only as

$$\frac{\mathrm{dh}}{\mathrm{dt}} = \mathbf{U} + \mathrm{K_m}\nabla^2\mathrm{h}\,, \tag{7}$$

where h is the topographic elevation, $\mathbf{U}$ the uplift rate and $\mathrm{K_m}$ the marine sediment diffusion coefficient.

Text S3: ASPECT/FastScape coupling

In this paper we use a two-way coupling of the tectonic ASPECT code and the landscape evolution FastScape code. For this coupling, a FastScape shared library is called by an ASPECT plugin to deform its surface as described in the previous section. The plugin has three main components: 1) Copy the surface height and velocity values from ASPECT. 2) Initialize and run FastScape at a resolution equivalent to or greater than the one used at the surface of ASPECT. If it is the first timestep of the tectonic model run, FastScape is initialized using height and velocity values from ASPECT. In subsequent timesteps, as FastScape runs separately and can be at a higher resolution than ASPECT, only the velocity values from ASPECT are transferred to FastScape. Before running FastScape, the initial topography values are saved. After running FastScape, the new and previous topography are compared to determine a nodal vertical (Z) velocity,

$$\mathbf{V_z} = \frac{\mathrm{h_c} - \mathrm{h_p}}{\mathrm{dt_a}}, \quad (8)$$

where $\mathrm{h_p}$ is the surface height at the start of the timestep (previous surface), and $\mathrm{h_f}$ the surface height after FastScape has been run (current surface), and $\mathrm{dt_a}$ the ASPECT timestep. 3) Using the overarching mesh deformation functionality (see Rose et al., 2017), the Z velocity field is interpolated onto the ASPECT surface to determine the displacement of the mesh surface and interior. From there, ASPECT responds to the change in topography calculated by FastScape due to the induced change in forces that is included in the Stokes equations. At the beginning of the next timestep, the updated velocities computed in the previous timestep are sent to FastScape once again.

The FastScape mesh includes an additional element-size layer of ghost nodes compared to the ASPECT surface mesh. The values of surface height on these nodes are not considered when interpolating the surface back to ASPECT and are used primarily to avoid FastScape boundary artifacts being sent to the ASPECT model (e.g., the boundaries do not uplift from advected topography). To avoid possible erroneous sediment flux out or into the model from artificial slopes, each timestep the ghost nodes are updated with the topography and velocity values of the nearest inward node (an ASPECT boundary node).

Besides passing ASPECT's uplift velocities, we use the plugin's FastScape interface to supply additional input to the surface process model in two ways: 1) to add marine background sedimentation via the sediment rain effect, and 2) to add a boundary sediment flux using the ghost nodes. For the sediment rain, at each nodal point we update FastScape with a flat height increase every ASPECT timestep. Through the diffusion component in equation (7), we prescribe a constant sediment flux at the boundary, assuming that

$$\mathbf{Q} = K_m S \,, \tag{9}$$

where **Q** is the sediment flux and S the slope. Since K_m and Q are user-set parameters, to achieve this we alter S by uplifting the boundary ghost nodes every ASPECT timestep so that **Q** remains constant.

Text S4: Model setup

In this study we examine how a strike-slip fault responds to sedimentation. We therefore set up a 3D box model with dimensions 100×8×120 km (X, Y, and Z, where Z is the vertical component) and 5 compositions representing a wet quartzite upper crust (Rutter and Brodie, 2004), wet anorthite lower crust (Rybacki et al., 2006), dry olivine lithospheric mantle, wet olivine asthenosphere (Hirth and Kohlstedt, 2003), and a sediment layer that has rheologic parameters identical to wet quartzite, but with density and temperature parameters consistent with sediment (Sippel et al., 2017). The total crustal thickness is set to 8 km (4 km upper crust, 4 km lower crust) based on crustal estimates of the area (7-10 km; Mahattanachai et al., 2021). The lithospheric mantle extends between the Moho and the lithosphere-asthenosphere boundary (LAB) at 40 km depth. The LAB depth, like the crust, has been perturbed by a previous extensional period. The remaining material beneath the LAB is considered asthenosphere (Fig. S1). While there is no initial sediment layer, the top boundary is fixed to a sediment composition so that any top-inflow of material due to topography changes other than uplift is sediment.

The ASPECT model mesh consists of two element sizes: 1 km and 2 km. The upper 8 km of the model is refined at 1 km to best resolve the crust and the forming sediment layer. This high-resolution area additionally extends to a depth of 35 k from X = 42 km to X = 52 km to better resolve the strike-slip fault. All other areas are kept at 2 km resolution.

The initial temperature above the LAB is determined by a steady-state geotherm (Turcotte and Schubert, 2013), and below by a mantle adiabat. For simplicity, an initial weak zone is seeded through a small perturbation: we raise the LAB locally by 10% of the lithospheric mantle thickness. We fix the top boundary temperature at 0 °C and the bottom boundary at the temperature initially determined from the mantle adiabat at that depth. All other boundaries are set to zero heat-flux.

The coupled model is run for 10 Myr, where the model in the first 5 Myr includes non-zero velocity boundary conditions. During this time, the western boundary is given a strike-slip component of 20 mm/yr (in Y), and an extensional component of 0.2 mm/yr (in X), while the Z-component of velocity is set to no-slip. This gives a total of 100 km of dextral strike-slip motion and 1 km of extension. The small extensional component is introduced to avoid compressional pop-ups that form at the shear zone as the lithosphere subsides due to the sediment load (Fig. S2). The exact extensional value is chosen to accommodate horizontal stress forces related to isostatic compensation. From 5-10 Myr, extension and strike-slip motion stop as the western boundary is set to no-slip in all directions. All other boundary conditions are constant for the entire model run, with the eastern boundary being no-slip in all directions, the north and south boundaries set to periodic to simulate an infinitely long strike-slip fault, the initial lithostatic pressure computed at a reference location prescribed on the bottom boundary to allow for outflow in response to sedimentation, and the top boundary deformed through the use of FastScape.

FastScape is set up with an arbitrarily high sea level so that the entire model is considered submarine. This setup leads to a model with no acting stream power law, and sediment being moved solely through marine sediment diffusion. For simplicity, we additionally assume that there is no compaction and no difference between sand and silt. As such, we use a diffusion coefficient of 500 m^2/y for both, a value consistent with open marine environments in previous modelling studies (e.g., Rouby et al., 2013). During the syn-strike-slip phase of the tectonic model (0-5 Myr) we supply sediment to the model in two ways: 1) To account for pelagic/hemipelagic sedimentation (sediment rain), we deposit at a constant and uniform sedimentation rate of 0.2 mm/yr. 2) We assume there is an asymmetric off-model source of sediment, similar to the eastern Mergui Ridge for the East Andaman Basin, that inputs sediment into the system from the eastern boundary at a rate of 40 m^2/yr. This is done through equation (9), wherein we uplift the ghost nodes at each timestep so that a constant flux is prescribed through marine diffusion. After this syn-tectonic stage spanning 5 Myr, sediment supply to the system is halted, although marine diffusion continues to work on the topography.

Parameter	Symbol	Units	Sediment	Upper crust	Lower crust	Lithospheric mantle	Asthenosphere
Reference density (at surface conditions)	ρ_0	kg m^{-3}	2520	2700	2850	3280	3300
Thermal expansivity	α	K^{-1}	$3.7\cdot10^{-5}$	$2.7\cdot10^{-5}$	$2.7\cdot10^{-5}$	$3.0\cdot10^{-5}$	$3.0\cdot10^{-5}$
Thermal diffusivity	κ	$m^2\ s^{-1}$	$7.28\cdot10^{-7}$	$9.26\cdot10^{-7}$	$5.85\cdot10^{-7}$	$8.38\cdot10^{-7}$	$8.33\cdot10^{-7}$
Heat capacity	C_p	J kg^{-1} K^{-1}	1200	1200	1200	1200	1200
Heat production	H	W m^{-3}	$1.2\cdot10^{-6}$	$1.5\cdot10^{-6}$	$0.2\cdot10^{-6}$	0	0
Cohesion	C	Pa	$20\cdot10^{6}$	$20\cdot10^{6}$	$20\cdot10^{6}$	$20\cdot10^{6}$	$20\cdot10^{6}$
Internal friction angle (unweakened)	ϕ	◦	30	30	30	30	30
Strain weakening interval	-	-	[0,1]	[0,1]	[0,1]	[0,1]	[0,1]
Strain weakening factor	ϕ_{wf}	-	0.25	0.25	0.25	0.25	0.25
Creep properties			Sediment	Wet quartzite	Wet anorthite	Dry olivine	Wet olivine
Stress exponent (dis)	n	-	4.0	4.0	3.0	3.5	3.5
Constant prefactor (dis)	A_{dis}	$Pa^{-n}\ s^{-1}$	$8.57\cdot10^{-28}$	$8.57\cdot10^{-28}$	$7.13\cdot10^{-18}$	$6.52\cdot10^{-16}$	$2.12\cdot10^{-15}$
Activation energy (dis)	E_{dis}	J mol^{-1}	$223\cdot10^{3}$	$223\cdot10^{3}$	$345\cdot10^{3}$	$530\cdot10^{3}$	$480\cdot10^{3}$
Activation volume (dis)	V_{dis}	m^3 mol^{-1}	0	0	$38\cdot10^{-6}$	$18\cdot10^{-6}$	$11\cdot10^{-6}$
Constant prefactor (diff)	A_{diff}	$Pa^{-1}\ s^{-1}$	$5.79\cdot10^{-19}$	$5.79\cdot10^{-19}$	$2.99\cdot10^{-25}$	$2.25\cdot10^{-9}$	$1.5\cdot10^{-9}$
Activation energy (diff)	E_{diff}	J mol^{-1}	$223\cdot10^{3}$	$223\cdot10^{3}$	$159\cdot10^{3}$	$375\cdot10^{3}$	$335\cdot10^{3}$
Activation volume (diff)	V_{diff}	m^3 mol^{-1}	0	0	$38\cdot10^{-6}$	$6\cdot10^{-6}$	$4\cdot10^{-6}$
Grain size (diff)	d	m	0.001	0.001	0.001	0.001	0.001
Grain size exponent (diff)	m	-	2.0	2.0	3.0	0	0

Table S1: ASPECT model parameters. Abbreviations: dis – dislocation creep, diff – diffusion creep.

Parameter	Symbol	Unit	Value
Marine sand transport coefficient	K_{sand}	m^2/yr	500
Surface sand porosity	φ_{sand}	-	0
Sand e-folding depth	z_{sand}	m	0
Marine silt transport coefficient	K_{silt}	m^2/yr	500
Surface silt porosity	φ_{silt}	-	0
Silt e-folding depth	z_{silt}	m	0
Sand-shale ratio	F	-	1
Thickness of transport layer	L	m	100
Sea level	h_{sea}	m	5000

Table S2: FastScape model parameters.

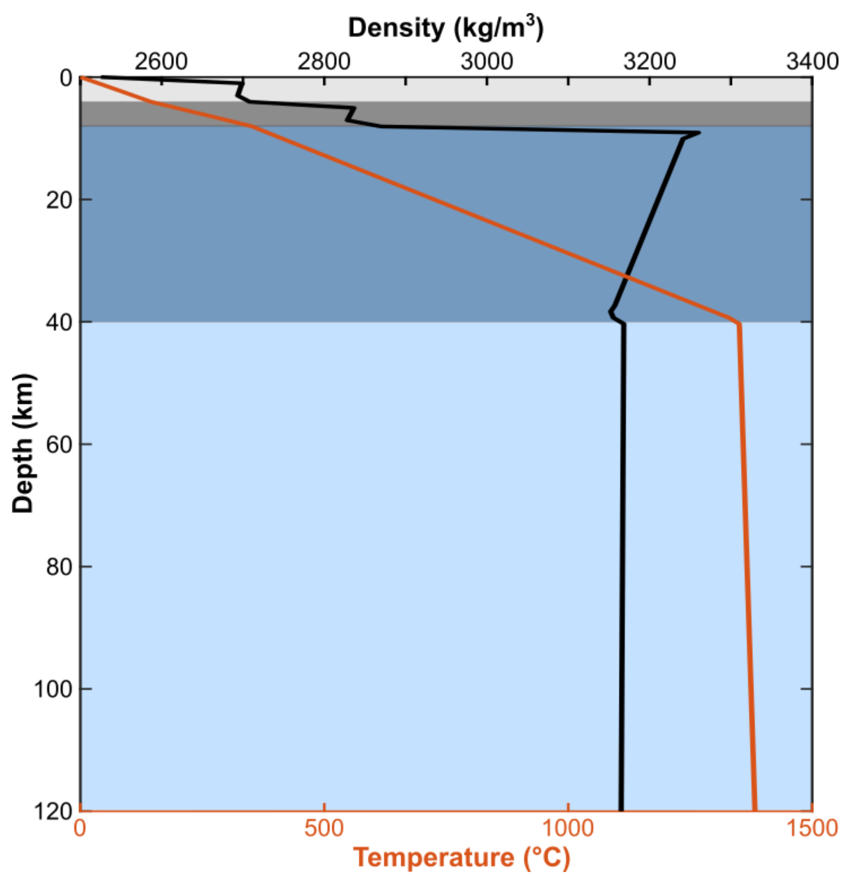

Figure S1: Initial density (black) and temperature (red) profiles with depth. Colored backgrounds represent the initial compositions, with light gray representing the upper crust, dark gray the lower crust, dark blue the mantle lithosphere, and light blue the asthenosphere.

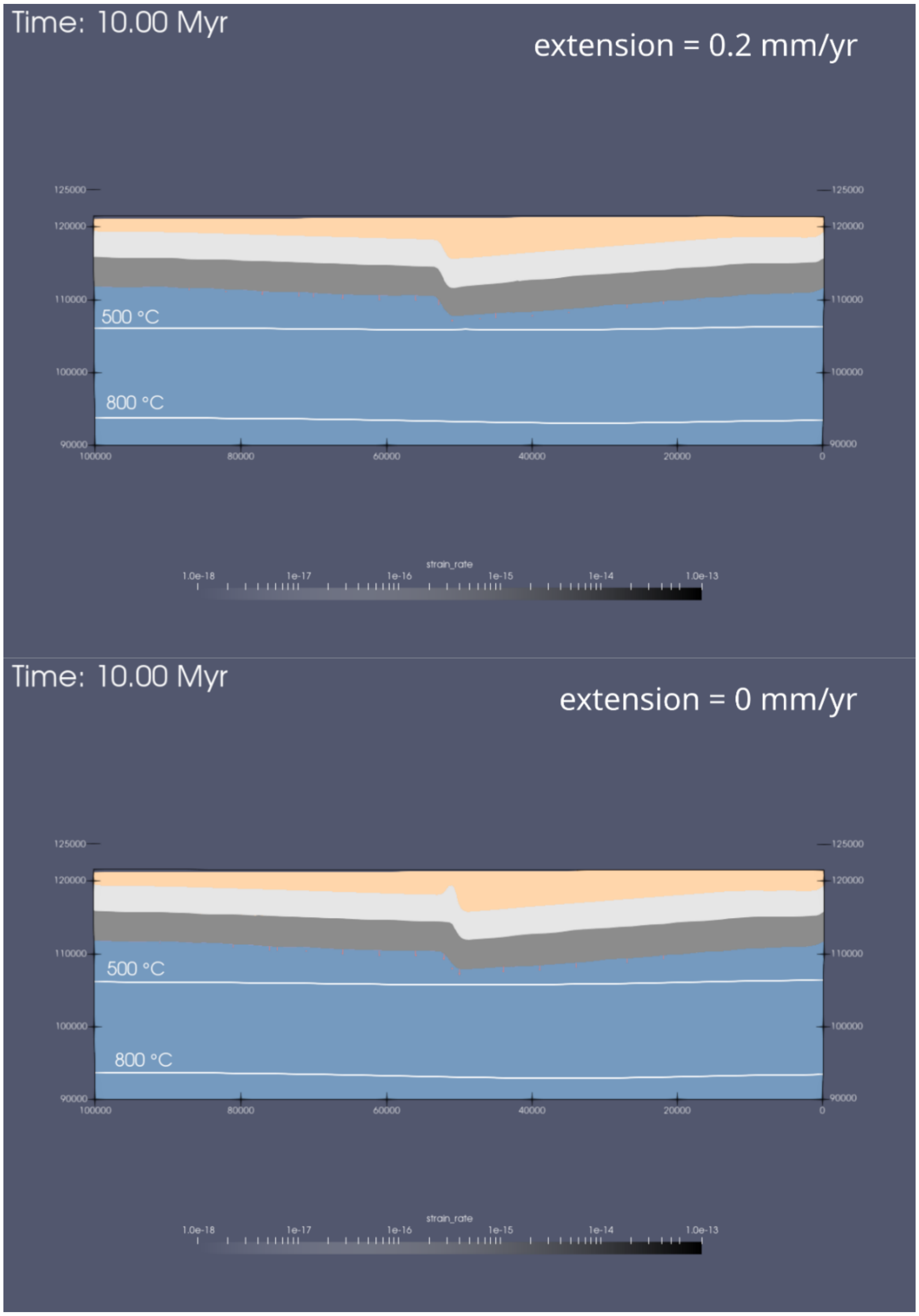

Figure S2: Comparison showing the reference model with A) a 0.2 mm/yr extensional component. B) no extensional component, leading to the formation of a small compressional pop-up in the center.

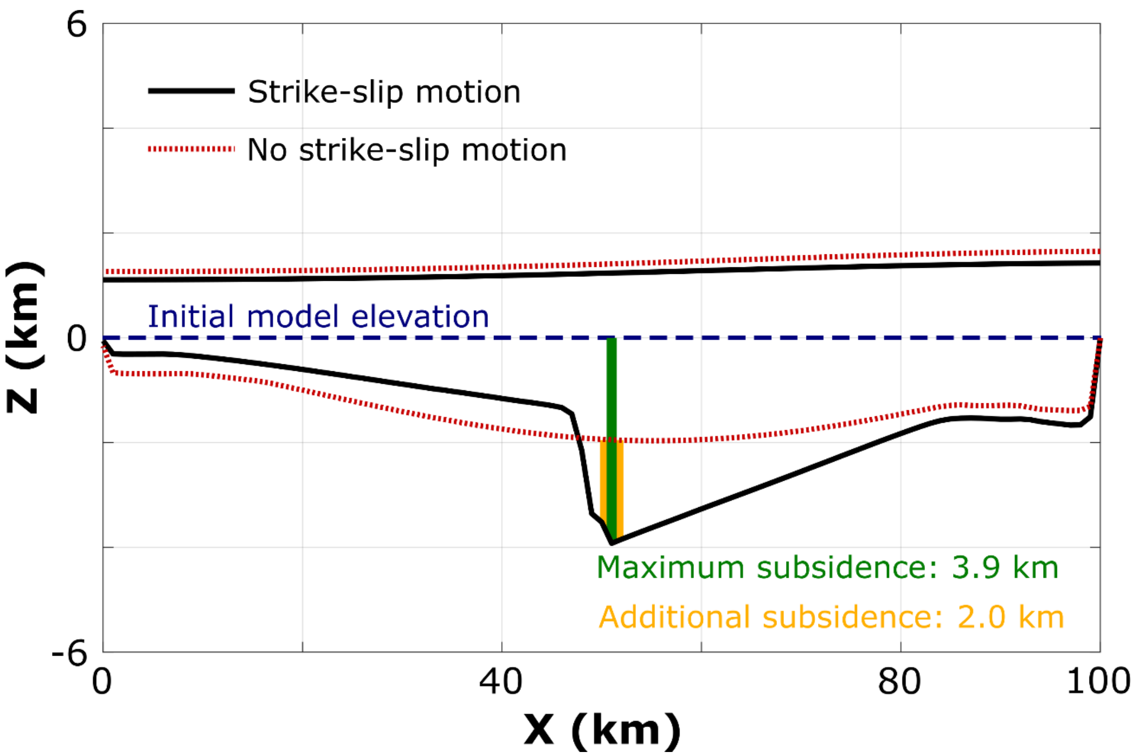

Figure S3: Comparison of the FastScape basement and topography from two models runs: The black curves represent the reference model; the dotted red curves show the reference model without strike-slip motion. The dashed blue line represents the initial model elevation, the green line indicates the total subsidence in the reference model with strike-slip motion, and the yellow line shows the difference in subsidence when comparing models with and without strike-slip motion. In the case without strike-slip motion, maximum subsidence and basin asymmetry are both greatly reduced.

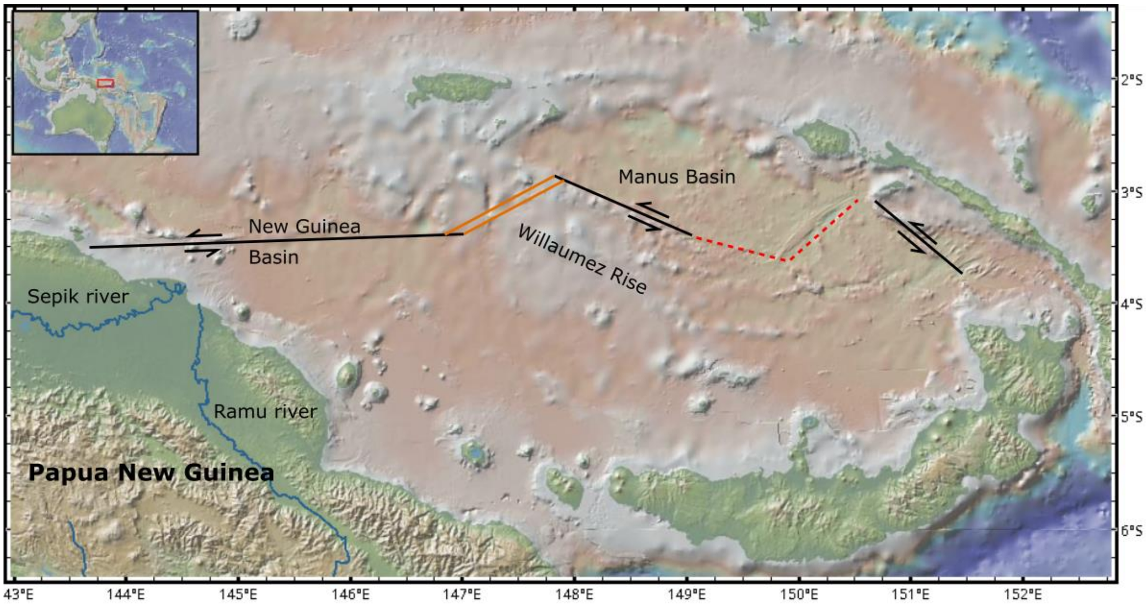

Figure S4: Regional map of the Manus back-arc region, with fault locations based on Fig. 1 in Martinez and Taylor, 1996. Black lines indicate strike-slip faults, parallel orange lines spreading centers, dashed red lines lava fields, and blue lines major rivers. This figure was made using GeoMappApp (www.geomapapp.org; Ryan et al., 2009).

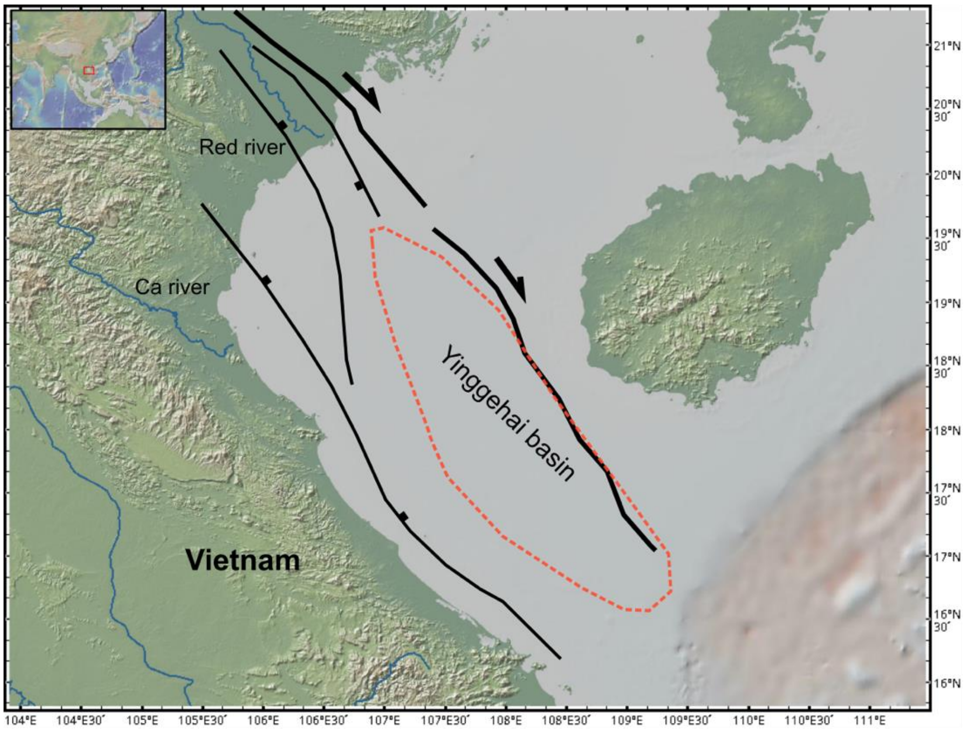

Figure S5: Regional map showing the Red River Fault Zone and location of the Yinggehai basin. Fault locations based on Fig. 10 in Noda, 2013. Black lines show faults, blue lines major rivers, and the Yinggehai basin is outlined in the dashed orange circle. This figure was made using GeoMappApp (www.geomapapp.org; Ryan et al., 2009).

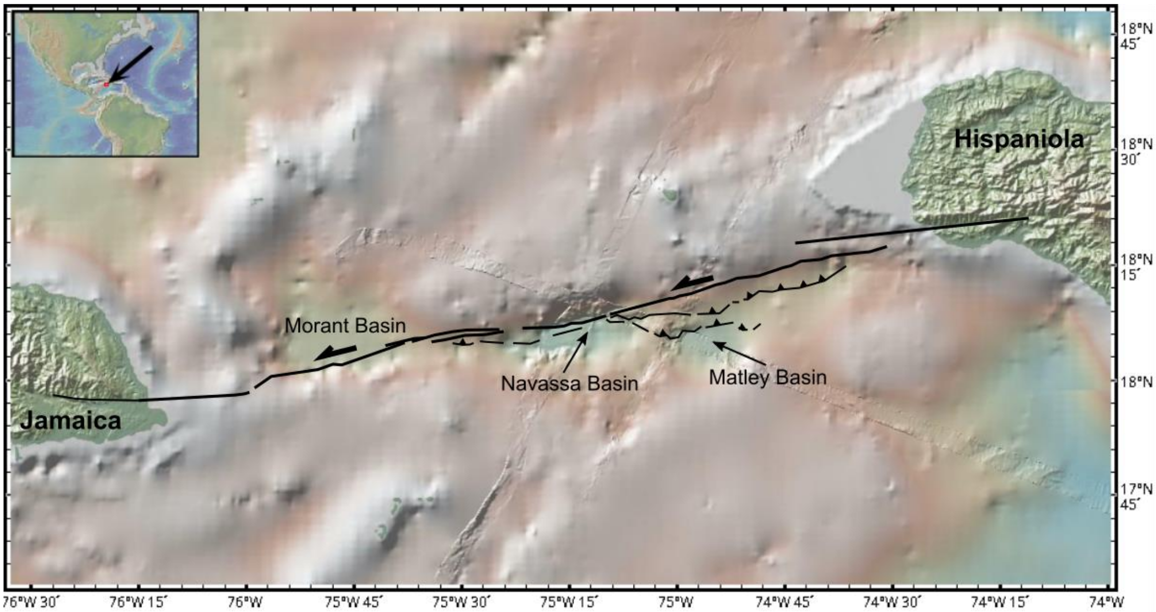

Figure S6: Regional map of the Jamaica Passage showing the Navassa strike-slip basin along the Enriquillo-Plantain-Garden Fault Zone. Fault locations based on Fig. 6 in Corbeau et al., 2016. This figure was made using GeoMappApp (www.geomapapp.org; Ryan et al., 2009).

Video S1: Full evolution of the tectonic reference model (Fig. 2C,K,G). Colors represent composition where tan is sediment, light gray is upper crust, dark gray is lower crust, dark blue is mantle lithosphere, and light blue is the asthenosphere. The white lines are temperature contours, gray-scale the strain rate, and arrows indicate the total velocity magnitude.

Video S2: Evolution of the middle slice of the top 30 km of the reference tectonic model. Colors represent composition where tan is sediment, light gray is upper crust, dark gray is lower crust, dark blue is mantle lithosphere, and light blue is the asthenosphere. The white lines are temperature contours, gray-scale the strain rate, and red arrows indicate the subsidence rate (Z velocity) along the 8 km depth contour.

References

Bangerth, W., Dannberg, J., Gassmoeller, R., and Heister, T., 2019, ASPECT v2.1.0: Zenodo, https://doi.org/10.5281/zenodo.2653531.

Braun, J., and Willett, S.D., 2013, A very efficient O(n), implicit and parallel method to solve the stream power equation governing fluvial incision and landscape evolution: Geomorphology, v. 180–181, p. 170–179, doi:10.1016/j.geomorph.2012.10.008.

Corbeau, J., Rolandone, F., Leroy, S., Mercier de Lépinay, B., Meyer, B., Ellouz-Zimmermann, N., and Momplaisir, R., 2016, The northern Caribbean plate boundary in the Jamaica Passage: Structure and seismic stratigraphy: Tectonophysics, v. 675, p. 209–226, doi:10.1016/j.tecto.2016.03.022.

Davis, R.O., and Selvadurai, A.P.., 2002, Plasticity and Geomechanics: Cambridge University Press.

Glerum, A., Thieulot, C., Fraters, M., Blom, C., and Spakman, W., 2018, Nonlinear viscoplasticity in ASPECT: Benchmarking and applications to subduction: Solid Earth, v. 9, p. 267–294, doi:10.5194/se-9-267-2018.

Heister, T., Dannberg, J., Gassmöller, R., and Bangerth, W., 2017, High Accuracy Mantle Convection Simulation through Modern Numerical Methods – II: Realistic Models and Problems.: Geophysical Journal International, v. 210, p. 833–851, doi:doi:10.1093/gji/ggx195.

Hirth, G., and Kohlstedt, D., 2003, Rheology of the upper mantle and the mantle wedge: a view from the experimentalists: Inside the Subudction Factory Geophysical Monograph (American Geophysical Union), v. 183.

Karato, S., and Wu, P., 1993, Rheology the Upper Mantle : Synthesis: v. 260.

Kronbichler, M., Heister, T., and Bangerth, W., 2012, High Accuracy Mantle Convection Simulation through Modern Numerical Methods.: Geophysical Journal International, v. 191, doi:doi:10.1111/j.1365-246x.2012.05609.x.

Mahattanachai, T., Morley, C.K., Charusiri, P., and Kanjanapayont, P., 2021, The Andaman Basin Central Fault Zone, Andaman Sea: Characteristics of a major deepwater strike-slip fault system in a polyphase rift: Marine and Petroleum Geology, p. 104997, doi:10.1016/j.marpetgeo.2021.104997.

Martinez, F., and Taylor, B., 1996, Backarc spreading, rifting, and microplate rotation, between transform faults in the Manus Basin: Marine Geophysical Researches, v. 18, p. 203–224, doi:10.1007/BF00286078.

Noda, A., 2013, Strike-Slip Basin – Its Configuration and Sedimentary Facies: Mechanism of

Sedimentary Basin Formation - Multidisciplinary Approach on Active Plate Margins, doi:10.5772/56593.

Rose, I., Buffett, B., and Heister, T., 2017, Stability and Accuracy of Free Surface Time Integration in Viscous Flows.: Physics of the Earth and Planetary Interiors, v. 262, p. 90–100, doi:doi:10.1016/j.pepi.2016.11.007.

Rouby, D., Braun, J., Robin, C., Dauteuil, O., and Deschamps, F., 2013, Long-term stratigraphic evolution of Atlantic-type passive margins: A numerical approach of interactions between surface processes, flexural isostasy and 3D thermal subsidence: Tectonophysics, v. 604, p. 83–103, doi:10.1016/j.tecto.2013.02.003.

Rutter, E.H., and Brodie, K.H., 2004, Experimental grain size-sensitive flow of hot-pressed Brazilian quartz aggregates: Journal of Structural Geology, v. 26, p. 2011–2023, doi:10.1016/j.jsg.2004.04.006.

Ryan, W.B.F. et al., 2009, Global Multi-Resolution Topography synthesis: Geochemistry, Geophysics, Geosystems, v. 10, doi:https://doi.org/10.1029/2008GC002332.

Rybacki, E., Gottschalk, M., Wirth, R., and Dresen, G., 2006, Influence of water fugacity and activation volume on the flow properties of fine-grained anorthite aggregates: Journal of Geophysical Research: Solid Earth, v. 111, doi:10.1029/2005JB003663.

Sippel, J., Meeßen, C., Cacace, M., Mechie, J., Fishwick, S., Heine, C., Scheck-Wenderoth, M., and Strecker, M., 2017, The Kenya rift revisited: Insights into lithospheric strength through data-driven 3-D gravity and thermal modelling: Solid Earth, v. 8, p. 45–81, doi:10.5194/se-8-45-2017.

Turcotte, D.L., and Schubert, G., 2013, Geodynamics: Cambridge University Press.

Yuan, X.P., Braun, J., Guerit, L., Rouby, D., and Cordonnier, G., 2019a, A New Efficient Method to Solve the Stream Power Law Model Taking Into Account Sediment Deposition: Journal of Geophysical Research: Earth Surface, v. 124, p. 1346–1365, doi:10.1029/2018JF004867.

Yuan, X.P., Braun, J., Guerit, L., Simon, B., Bovy, B., Rouby, D., Robin, C., and Jiao, R., 2019b, Linking continental erosion to marine sediment transport and deposition: A new implicit and O(N) method for inverse analysis: Earth and Planetary Science Letters, v. 524, p. 115728, doi:10.1016/j.epsl.2019.115728.